

Probing Site-Resolved Current in Strongly Interacting Superconducting Circuit Lattices

Botao Du, Ramya Suresh, Santiago López, Jeremy Cadiente, and Ruichao Ma*
Department of Physics and Astronomy, Purdue University, West Lafayette, IN 47907, USA
 (Dated: March 18, 2024)

Transport measurements are fundamental for understanding condensed matter phenomena, from superconductivity to the fractional quantum Hall effect. Analogously, they can be powerful tools for probing synthetic quantum matter in quantum simulators. Here we demonstrate the measurement of in-situ particle current in a superconducting circuit lattice and apply it to study transport in both coherent and bath-coupled lattices. Our method utilizes controlled tunneling in a double-well potential to map current to on-site density, revealing site-resolved current and current statistics. We prepare a strongly interacting Bose-Hubbard lattice at different lattice fillings, and observe the change in current statistics as the many-body states transition from superfluid to Mott insulator. Furthermore, we explore non-equilibrium current dynamics by coupling the lattice to engineered driven-dissipative baths that serve as tunable particle source and drain. We observe steady-state current in discrete conduction channels and interaction-assisted transport. These results establish a versatile platform to investigate microscopic quantum transport in superconducting circuits.

Charge transport is at the heart of condensed matter physics. Electrical conductivity measurements are used to probe the intrinsic properties of charge carriers and advance our understanding of quantum phases and phase transitions [1]. Meanwhile, current fluctuations in shot-noise measurements can help reveal the quantum dynamics and correlations of charge carriers in strongly interacting systems [2].

Synthetic quantum matter are emerging platforms for quantum simulation of condensed matter models, providing pristine many-body systems with exquisite control, tunability, and measurement capabilities [3–5]. However, conventional transport measurements in synthetic quantum matter are often challenging due to their finite system sizes and isolated nature. For example, transport properties in ultracold atomic gases are typically extracted from the time evolution of particle density either in response to an engineered non-uniform initial density [6, 7] or to applied external forces [8]. The particle current through an atomic quantum point contact was measured by monitoring the particle number change in the attached finite-size reservoirs [9, 10].

In superconducting (SC) quantum circuits, arrays of coupled SC qubits and resonators realize lattice models to study synthetic quantum matter comprised of interacting microwave photons [11–14]. Recent experiments have explored quantum states and dynamics in Bose-Hubbard lattices [15–19], many-body localization [20–22], entanglement generation and characterization [23–25], and flat-band physics [26, 27]. Coherent transport of microwave photons has been probed via density measurements in a disordered lattice [22], and chiral current was directly measured in a triangular unit-cell with synthetic magnetic field [28]. SC circuits also provide an ideal playground to investigate non-equilibrium transport in driven-dissipative lattices [29–32], with recent experiments performing microwave transmission spectroscopy

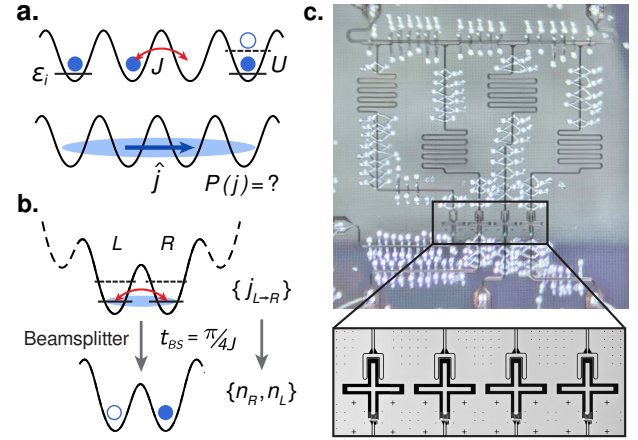


FIG. 1. Measurement scheme. (a) Illustration of a strongly interacting Bose-Hubbard lattice, and the particle current between two neighboring lattice sites. (b) Controlled tunneling in the double-well potential realizes a beamsplitter operation that maps the nearest-neighbor current to on-site density. (c) Image of the superconducting circuit device with a zoomed-in view of the four-site transmon qubit lattice.

of driven-dissipative phases in 1D lattices [33–35].

In this Letter, we demonstrate the measurement of in-situ particle current in a SC circuit lattice, with direct access to site-resolved current and current statistics. Our method is based on the scheme in [36] and adapted to work for strongly interacting particles. We measure current statistics in the Bose-Hubbard lattice coherently prepared at different fillings, and study non-equilibrium current dynamics in a bath-coupled lattice.

Measurement Scheme. We consider a Bose-Hubbard lattice (Fig. 1a) described by the Hamiltonian:

$$\mathcal{H}_{\text{BH}}/\hbar = \sum_{\langle ij \rangle} J a_i^\dagger a_j + \frac{U}{2} \sum_i n_i(n_i - 1) + \sum_i \epsilon_i n_i$$

where a_i^\dagger is the bosonic creation operator for a particle on site i , J is the nearest neighbor tunneling rate, U is the on-site interaction, $n_i = a_i^\dagger a_i$ is the on-site occupancy, ϵ_i is the local on-site energy, and \hbar is the reduced Planck constant. The current operator $\hat{j}_{l \rightarrow r}$ for particles flowing from site l to site r is defined, from the continuity equation for local particle density, as [36]:

$$\hat{j}_{l \rightarrow r} = iJ(a_l^\dagger a_r - a_r^\dagger a_l)$$

For non-interacting particles ($U \approx 0$), the current can be measured using an effective beamsplitter operation (BS) implemented as controlled resonant tunneling between the two sites [36], illustrated in Fig. 1b. After the evolution of an initial state in the isolated two-site system for a duration of $t_{\text{BS}} = \pi/4J$, the initial current is mapped onto density imbalance according to $\hat{j}_{l \rightarrow r} \xrightarrow{\text{BS}} J(n_r - n_l)$. As indicated from this mapping, the current operator \hat{j} has discrete eigenvalues $j \in \{-nJ, -(n-1)J, \dots, +nJ\}$, where $n = n_l + n_r$ is the total number of particles on the two sites. The current expectation value $\langle j \rangle$ and current statistics $P(j)$ are then extracted from a particle-number-resolved density measurement after the beamsplitter operation. This recipe applies to systems where interaction is weak or can be turned off. It was implemented in ultracold atoms to probe chiral currents albeit without spatial resolution [37] and recently in a quantum gas microscope to measure local current and current correlations [38].

Here, we extend this method to strongly interacting lattices in the hard-core boson limit ($U \gg J$). The on-site occupancy cannot exceed $n_i = 1$ under the hard-core condition, thereby limiting the current eigenvalues to $j \in \{-2J, -J, 0, +J, +2J\}$. We denote the on-site Fock states as $|0\rangle$ and $|1\rangle$. With the same resonant tunneling of duration t_{BS} between two sites, now in the presence of large U , the current eigenstates corresponding to $j = \{-J, 0, +J\}$ map uniquely to Fock states $\{|10\rangle, |00\rangle, |01\rangle\}$ after the beamsplitter, i.e. $P(j = -J) \xrightarrow{\text{BS}} P(|10\rangle)$ etc. The Fock state $|11\rangle$ does not evolve in density during the beamsplitter operation in the hard-core limit, and can be written as an equal superposition of current eigenstates for $j = \pm 2J$. Therefore we obtain the probability of the remaining current components as $P(j = \pm 2J) \xrightarrow{\text{BS}} \frac{1}{2}P(|11\rangle)$. This protocol for measuring current is tailored for analog quantum simulation experiments in SC circuits, as it only requires density readout and does not rely on measuring phase-sensitive correlation functions. See Supplementary Material (SM) Sec. D for a detailed derivation of the current measurement.

SC circuit Bose-Hubbard lattice. In our SC circuit device, four transmon qubits [39] constitute the lattice sites of the 1D Bose-Hubbard lattice (Fig. 1c). The capacitive coupling between neighboring transmons results in tunneling $J \approx 2\pi \times 6$ MHz, while the transmon anharmonicity provides the effective on-site interaction

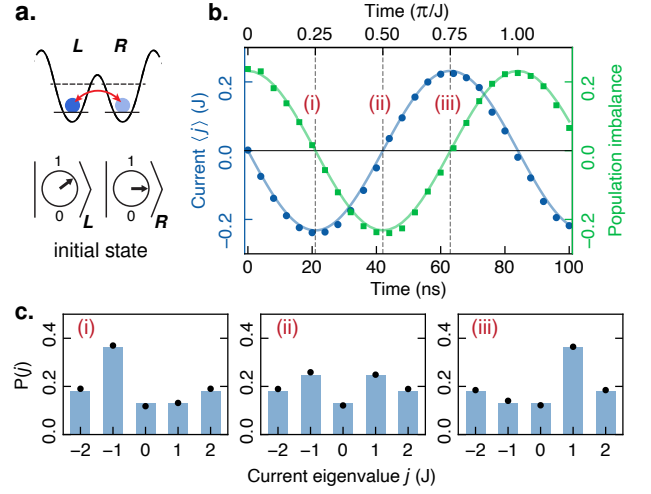


FIG. 2. Current dynamics in a resonant double-well. (a) We start in a product state of two sites with unequal population. (b) Time evolution of current and population imbalance in the strongly interacting two-site system. (c) Current statistics at three different evolution times. Solid lines in (b) and bars in (c) are results from numerical simulation. Data shown in all figures are typically averaged over 40,000-100,000 experimental runs, with standard error of the mean smaller than the size of the data points. Other systematic uncertainties in the extracted density or current are below $\pm 1\%$, see SM Sec. C.

$U \approx -2\pi \times 246$ MHz. The on-site energies ϵ_i are given by the frequency of the transmon $n = 0 \rightarrow 1$ transition ω_q and dynamically tunable via individual on-chip flux lines. We typically operate the lattice near $\omega_q \approx 2\pi \times 4.5$ GHz. Microwave photons in the lattice (transmon excitations) have a relaxation rate of $\Gamma_1 = 1/T_1 \approx 2\pi \times 5$ kHz and a dephasing rate of $\Gamma_\phi = 1/T_2^* \approx 2\pi \times 60$ kHz. Each transmon lattice site is capacitively coupled to an individual coplanar waveguide resonator used for dispersive readout of the on-site occupancy. We simultaneously measure all lattice sites by performing frequency-multiplexed readout via a common readout transmission line. See SM Sec. A-C for details on device parameters, measurement setup, and lattice control and characterization.

Current dynamics in a double-well. To illustrate our protocol, we measure the current and current statistics in a resonant double-well formed by two neighboring transmon lattice sites (Fig. 2a). We start with the two sites far-detuned in frequency in their equilibrium ground states, which have approximately 6% thermal population in $|1\rangle$ due to the finite effective temperature of the device. By applying a resonant microwave pulse on each transmon, we choose to prepare a product state of the left and right sites with initial $P(|1\rangle)$ of 76% and 50% respectively. The coherent microwave pulses correspond to X -rotations of 127° and 90° on the Bloch sphere of the transmon qubits. We then rapidly bring the two sites into resonance and evolve for a variable time before applying the current measurement protocol. The data is shown

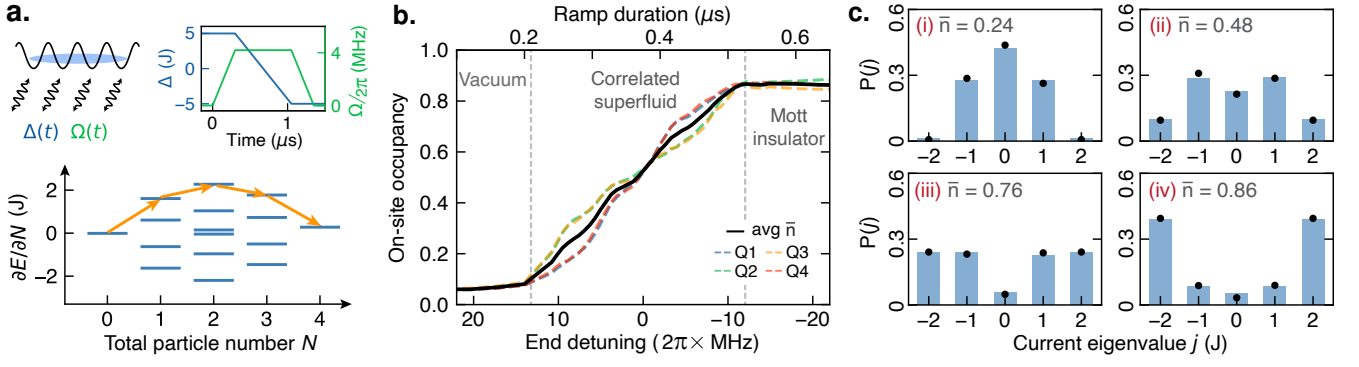


FIG. 3. Current statistics in a coherent Bose-Hubbard lattice. (a) Many-body states with different lattice fillings are prepared using a global coherent drive with time-varying amplitude and detuning. As the drive detuning varies, the lattice is adiabatically filled through a sequence of transitions in the many-body spectrum (orange arrows). (b) The measured on-site occupancy and average filling as a function of the drive end detuning. (c) Current statistics at four different lattice fillings, showing the change in the probability distribution. Bars show results from numerical simulation.

in Fig. 2b where we observe the coherent oscillation of the current $\langle j_{L \rightarrow R} \rangle$ with a period of π/J . Separately, we measure the on-site density in the double-well and observe the population imbalance $\langle n_R - n_L \rangle$ oscillating 90° out of phase with the current, as expected from the relation between current and density under resonant tunneling discussed above. In this experiment, the density and current measurements share the same pulse sequence with the latter evolving for an extra duration of t_{BS} in the double-well. The measured current statistics $P(j)$ at three different times are plotted in Fig. 2c, revealing the origin of the observed current expectation value and its quantum fluctuations. The oscillating non-zero current results from the changing contributions from the $j = \pm J$ components, while the $j = \pm 2J$ components remain constant due to the hard-core condition. See SM Sec. D for calibration of the beamsplitter operation.

Current statistics in Bose-Hubbard lattice. We investigate current statistics in the hard-core Bose-Hubbard lattice at different average fillings $0 < \bar{n} \leq 1$. At unit filling, the state corresponds to the Mott insulator phase with suppressed density fluctuations [40]. At partial filling, the states are correlated superfluids where strong on-site interaction induces repulsive density correlations in the limit of 1D Tonks–Girardeau gases [18]. SC circuits provide a platform for new approaches to creating strongly correlated quantum states. Many-body states can be prepared spectroscopically via direct driving [25, 41], or with disorder-assisted local adiabatic control [18]. Alternatively, engineered dissipation can serve as an effective chemical potential for microwave photons to stabilize many-body phases in SC circuits [42–44].

Here we prepare the Bose-Hubbard lattice at different fillings via adiabatic many-body Landau-Zener transitions using coherent external driving, similar to methods employed in recent Rydberg atom experiments [45]. As illustrated in Fig. 3a, we apply a global microwave

drive to all lattice sites via the readout transmission line. Starting with an empty lattice, we turn on the coherent drive to a Rabi amplitude $\Omega \approx 2\pi \times 4.2$ MHz in 300 ns. The initial drive frequency is detuned by $\Delta = 2\pi \times 30$ MHz $\approx 5J$ above the lattice frequency, away from all single-particle resonances which are within $\pm 2J$ of the lattice frequency. We then ramp the drive frequency at a constant rate of $-2\pi \times 80$ MHz/ μ s to populate the lattice through a sequence of avoided crossings between states of different total particle number N . The drive detuning at the end of the ramp is varied and determines the final lattice filling \bar{n} . Due to the relatively uniform drive amplitude and phase across the lattice sites, we prepare the highest energy states at different \bar{n} . Finally, we ramp down the drive amplitude to zero in 300 ns and then measure the resulting many-body state. Figure 3b shows the measured on-site occupancy and average lattice filling as a function of the drive end detuning. The final state transitions from the empty vacuum, to strongly-interacting superfluids at partial filling, to the Mott insulator at unit filling. To verify the adiabaticity of the preparation, we perform the coherent drive twice with a second reversed detuning ramp and measure the final lattice density. Due to finite thermal population, the lattice starts with $P(|0000\rangle) \approx 80\%$, and we extract a return probability of $P(|0000\rangle) \approx 60\%$ after the double ramp by comparing density data to numerical simulations. The preparation fidelity is consistent with theory and primarily limited by decoherence in the lattice. See SM Sec. E for the design and characterization of the drive parameters and additional analysis on adiabaticity.

The current statistics at different lattice fillings, measured between the two middle lattice sites, are shown in Fig. 3c. For low filling $\bar{n} = 0.24$ ($N \approx 1$), a single microwave photon is delocalized over the lattice, with strong fluctuations of the on-site occupancy. The current statistics is expected to follow a Skellam distribu-

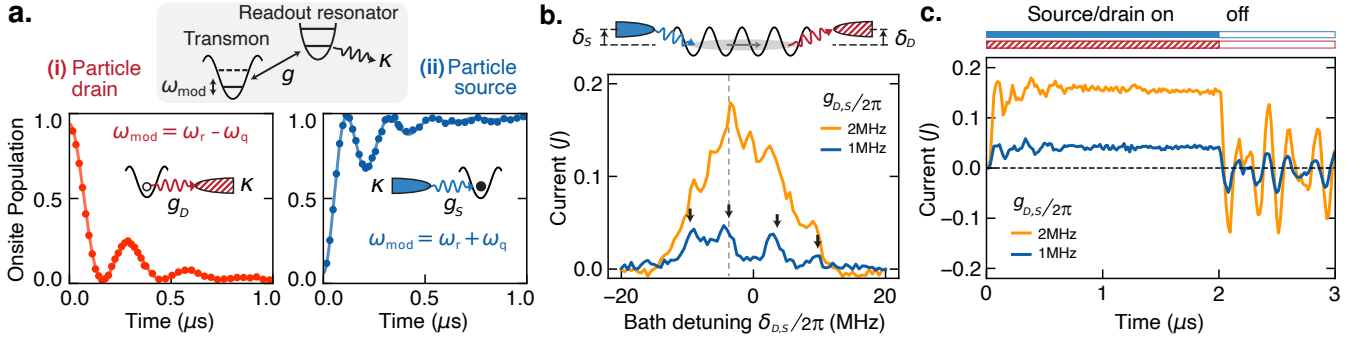


FIG. 4. Transport in a bath-coupled lattice. (a) We engineer local particle drain (i) and source (ii) by parametric coupling of the transmon and the lossy readout resonator. Plots show the dynamics of a single site coupled to the drain or source. Dots are experimental data; lines are numerical simulations. (b) Steady-state current through the lattice with end-coupled source and drain, measured as a function of bath detuning for two bath coupling rates. Black arrows on the current plot indicate frequencies of the single-particle eigenstates. (c) Time dynamics of the current with the baths turned on at $t = 0$, then turned off at $t = 2\text{ }\mu\text{s}$ after reaching steady state. The bath detuning in (c) is indicated by the dotted line in (b).

tion [36] with a broad distribution peaked at $j = 0$. As \bar{n} increases, both the density and current fluctuations are increasingly suppressed due to the strong interaction U . The observed $P(j)$ gradually becomes peaked at two eigenvalues $j = \pm 2J$, as a result of the Mott insulator at $\bar{n} = 1$ being the equal superposition of current eigenstates $j = \pm 2J$. The adiabatically prepared stationary states all have a vanishing mean current $\langle j \rangle$, as reflected in the symmetric distribution of the measured current statistics. The current statistics vary slightly at different locations in a finite lattice but have the same qualitative features.

Current in a bath-coupled lattice. Finally, we explore particle transport in open lattices that are difficult to access in closed quantum systems or by local density measurements alone. We couple the two ends of the Bose-Hubbard lattice to particle source and drain, and measure current through the interacting 1D system. Such boundary-driven transport has been the subject of many recent theoretical investigations [46, 47].

We utilize the transmon readout resonators as the source of dissipation to engineer local particle baths. The far-detuned resonators, with frequency $\omega_r \sim 2\pi \times (6.1 - 6.3)$ GHz and linewidth $\kappa \approx 2\pi \times 1.5$ MHz, are coupled to each transmon with $g \approx 2\pi \times 65$ MHz (Fig. 4a). We generate resonant interactions between the transmon site and the resonator by parametric driving of the transmon flux line at frequency ω_{mod} . When $\omega_{\text{mod}} \approx \omega_r - \omega_q$, the flux driving modulates the on-site frequency and induces a coherent modulation-assisted tunneling between the transmon site and the resonator [48, 49]. Since the resonator is lossy, this leads to an effective drain for microwave photons in the lattice. Alternatively when $\omega_{\text{mod}} \approx \omega_r + \omega_q$, the coherent parametric drive creates a pair of excitations, one to the transmon and one to the resonator [50]. One of the two excitations is lost via the resonator, leaving the other incoherently added to

the transmon site – this leads to a particle source. We hence realize a hardware-efficient implementation of local baths anywhere in the lattice. The drain (D) and source (S) both have a narrow energy bandwidth of $\kappa \ll J$. The effective bath-lattice coupling rates $g_{D,S}$ and effective bath-lattice detunings $\delta_{D,S} = (|\omega_{\text{mod}} - \omega_r| - \omega_q)$ are dynamically tunable by controlling the amplitude and frequency of the parametric drive respectively. Similar parametric driving processes are widely used in SC circuits for engineering tunable interactions [48–53].

In Fig. 4a(i), we plot the measured dynamics of an isolated site coupled resonantly to the drain with $\delta_D = 0$ and $g_D = 2\pi \times 1.75$ MHz. The site is initialized with one photon and relaxes via its coupling with the drain to a steady-state population of $P(|1\rangle) = 0.02$, limited by the resonator thermal population. In (ii), an initially empty site is coupled to the source with $\delta_S = 0$ and $g_S = 2\pi \times 2.4$ MHz where the on-site population reaches a steady-state value of $P(|1\rangle) = 0.98$ in about $1\text{ }\mu\text{s}$. In this device, we achieve maximum coupling rates of $g_D \sim 2\pi \times 12$ MHz limited by the flux tuning range of the transmon, and $g_S \sim 2\pi \times 4$ MHz limited by drive-induced heating.

To probe energy-dependent transport through the Bose-Hubbard lattice, we couple the source and drain to the ends of our 1D lattice with the same coupling rates and same detunings from the lattice (Fig. 4b). After turning on the baths for $2\text{ }\mu\text{s}$, we apply the current measurement protocol to the middle two lattice sites to measure the steady-state current $\langle j \rangle$ as a function of the bath detuning. At a relatively weak bath coupling of $g_{D,S} = 2\pi \times 1$ MHz, we observe four distinct current peaks when the narrow-band baths are tuned near the frequencies of the four single-particle eigenstates (i.e. $N=1$ states in Fig. 3a). Since the current operator commutes with particle number [36], states with different total particle number contribute to the current independently. Therefore, a non-zero steady-state current

implies some coherent superposition between eigenstates with the same particle number. For weak bath coupling and low lattice filling, we expect the coherent admixture to mainly result from off-resonant excitation of different single-particle eigenstates by the finite bandwidth bath. At a stronger bath coupling of $g_{D,S} = 2\pi \times 2$ MHz, we observe higher steady-state currents over a broader range of bath detuning. The effective broadening of the baths at higher coupling rates enables more many-body eigenstates to participate in the transport. For example, the additional peaks in the measured current at higher $g_{D,S}$ can be associated with processes involving several multi-particle states at different energies. Such non-linear transport processes are assisted by the bath coupling and by the effective interaction between many-body states induced by on-site interaction U .

In Fig. 4c, we measure the time evolution of the current at the specific bath detuning of $\delta_{D,S} = -2\pi \times 4$ MHz. After the source and drain are turned on at $t = 0$, we observe currents with initial oscillations that settle to the steady state within $1 \mu\text{s}$. At $t = 2 \mu\text{s}$, we turn off both baths and observe the subsequent coherent oscillations of the current. The many-body states are now evolving in an isolated lattice, resulting in a time-averaged net current of zero. In bath-coupled lattices, the non-equilibrium many-body state depends sensitively on the interplay between the coherent lattice interactions and parameters of the driven-dissipative baths [54–56]. Our future work will explore the detailed dependence of the steady-state current and current dynamics on the bath's spectral properties, lattice disorder and decoherence, and many-body interactions.

Conclusion. In this Letter, we demonstrated site-resolved current and current statistics measurement in a strongly interacting SC circuit lattice. We leveraged both coherent control and engineered driven-dissipation to generate many-body states and dynamics in the Bose-Hubbard lattice, establishing a versatile setup for future exploration of out-of-equilibrium transport in open quantum systems and quantum thermodynamics [57, 58]. Energy-dependent transport using tunable baths can probe critical behavior that is sometimes masked by transient finite-size effects in small closed systems [59]. Measuring current in the quantum critical regime, where the quasiparticle picture breaks down, will provide insights into the nature of collective excitations, how dissipation influences quantum critical dynamics, and how quantum entanglement evolves. For example, current statistics can reveal correlations and entanglement in many-body systems [60]. Furthermore, complex current correlation functions can be measured by simultaneous readout of multiple pairs of sites to investigate topological properties, e.g., in 2D lattices with chiral edge states [61, 62].

We would like to thank Qi Zhou for stimulating discussions, and Srivatsan Chakram and Andrei Vrajitoarea for a careful reading of the manuscript. This work was sup-

ported by grants from the National Science Foundation (award number DMR-2145323) and the Army Research Office (award number FA9550-23-1-0491).

* maruichao@purdue.edu

- [1] S. Sachdev, *Quantum Phase Transitions* (Cambridge University Press, 2011).
- [2] Y. Blanter and M. Büttiker, *Physics Reports* **336**, 1–166 (2000).
- [3] I. Georgescu, S. Ashhab, and F. Nori, *Reviews of Modern Physics* **86**, 153–185 (2014).
- [4] E. Altman, K. R. Brown, G. Carleo, L. D. Carr, E. Demler, C. Chin, B. DeMarco, S. E. Economou, M. A. Eriksson, K.-M. C. Fu, M. Greiner, K. R. Hazzard, R. G. Hulet, A. J. Kollár, B. L. Lev, M. D. Lukin, R. Ma, X. Mi, S. Misra, C. Monroe, K. Murch, Z. Nazario, K.-K. Ni, A. C. Potter, P. Roushan, M. Saffman, M. Schleier-Smith, I. Siddiqi, R. Simmonds, M. Singh, I. Spielman, K. Temme, D. S. Weiss, J. Vučković, V. Vuletić, J. Ye, and M. Zwierlein, *PRX Quantum* **2** (2021).
- [5] A. J. Daley, I. Bloch, C. Kokail, S. Flannigan, N. Pearson, M. Troyer, and P. Zoller, *Nature* **607**, 667–676 (2022).
- [6] J.-Y. Choi, S. Hild, J. Zeiher, P. Schauß, A. Rubio-Abadal, T. Yefsah, V. Khemani, D. A. Huse, I. Bloch, and C. Gross, *Science* **352**, 1547–1552 (2016).
- [7] P. T. Brown, D. Mitra, E. Guardado-Sanchez, R. Nourafkan, A. Reymbaut, C.-D. Hébert, S. Bergeron, A.-M. S. Tremblay, J. Kokalj, D. A. Huse, P. Schauß, and W. S. Bakr, *Science* **363**, 379 (2019).
- [8] R. Anderson, F. Wang, P. Xu, V. Venu, S. Trotzky, F. Chevy, and J. H. Thywissen, *Physical Review Letters* **122** (2019).
- [9] J.-P. Brantut, J. Meineke, D. Stadler, S. Krinner, and T. Esslinger, *Science* **337**, 1069 (2012).
- [10] S. Häusler, S. Nakajima, M. Lebrat, D. Husmann, S. Krinner, T. Esslinger, and J.-P. Brantut, *Physical Review Letters* **119** (2017).
- [11] C. Noh and D. G. Angelakis, *Reports on Progress in Physics* **80**, 016401 (2016).
- [12] M. J. Hartmann, *Journal of Optics* **18**, 104005 (2016).
- [13] X. Gu, A. F. Kockum, A. Miranowicz, Y. xi Liu, and F. Nori, *Physics Reports* **718–719**, 1 (2017).
- [14] I. Carusotto, A. A. Houck, A. J. Kollár, P. Roushan, D. I. Schuster, and J. Simon, *Nature Physics* **16**, 268–279 (2020).
- [15] S. Hacothen-Gourgy, V. Ramasesh, C. D. Grandi, I. Siddiqi, and S. Girvin, *Physical Review Letters* **115** (2015).
- [16] M. C. Collodo, A. Potočnik, S. Gasparinetti, J.-C. Besse, M. Pechal, M. Sameti, M. J. Hartmann, A. Wallraff, and C. Eichler, *Physical Review Letters* **122** (2019).
- [17] R. Ma, B. Saxberg, C. Owens, N. Leung, Y. Lu, J. Simon, and D. I. Schuster, *Nature* **566**, 51 (2019).
- [18] B. Saxberg, A. Vrajitoarea, G. Roberts, M. G. Panetta, J. Simon, and D. I. Schuster, *Nature* **612**, 435 (2022).
- [19] A. Morvan, T. I. Andersen, X. Mi, C. Neill, A. Petukhov, K. Kechedzhi, D. A. Abanin, A. Michailidis, R. Acharya, F. Arute, K. Arya, A. Asfaw, J. Atalaya, J. C. Bardin, J. Basso, A. Bengtsson, G. Bortoli, A. Bourassa, J. Bova, L. Brill, M. Broughton, B. B. Buckley, D. A. Buell, T. Burger, B. Burkett, N. Bushnell, Z. Chen,

- B. Chiaro, R. Collins, P. Conner, W. Courtney, A. L. Crook, B. Curtin, D. M. Debroy, A. D. T. Barba, S. Demura, A. Dunsworth, D. Eppens, C. Erickson, L. Faoro, E. Farhi, R. Fatemi, L. F. Burgos, E. Forati, A. G. Fowler, B. Foxen, W. Giang, C. Gidney, D. Gilboa, M. Giustina, A. G. Dau, J. A. Gross, S. Habegger, M. C. Hamilton, M. P. Harrigan, S. D. Harrington, M. Hoffmann, S. Hong, T. Huang, A. Huff, W. J. Huggins, S. V. Isakov, J. Iveland, E. Jeffrey, Z. Jiang, C. Jones, P. Juhas, D. Kafri, T. Khattar, M. Khezri, M. Kieferová, S. Kim, A. Y. Kitaev, P. V. Klimov, A. R. Klots, A. N. Korotkov, F. Kostitsa, J. M. Kreikebaum, D. Landhuis, P. Laptev, K.-M. Lau, L. Laws, J. Lee, K. W. Lee, B. J. Lester, A. T. Lill, W. Liu, A. Locharla, F. Malone, O. Martin, J. R. McClean, M. McEwen, B. M. Costa, K. C. Miao, M. Mohseni, S. Montazeri, E. Mount, W. Mruczkiewicz, O. Naaman, M. Neeley, A. Nersisyan, M. Newman, A. Nguyen, M. Nguyen, M. Y. Niu, T. E. O'Brien, R. Olenewa, A. Opremcak, R. Potter, C. Quintana, N. C. Rubin, N. Saei, D. Sank, K. Sankaragomathi, K. J. Satzinger, H. F. Schurkus, C. Schuster, M. J. Shearn, A. Shorter, V. Shvarts, J. Skrzynny, W. C. Smith, D. Strain, G. Sterling, Y. Su, M. Szalay, A. Torres, G. Vidal, B. Villalonga, C. Vollgraf-Heidweiller, T. White, C. Xing, Z. Yao, P. Yeh, J. Yoo, A. Zalcman, Y. Zhang, N. Zhu, H. Neven, D. Bacon, J. Hilton, E. Lucero, R. Babbush, S. Boixo, A. Megrant, J. Kelly, Y. Chen, V. Smelyanskiy, I. Aleiner, L. B. Ioffe, and P. Roushan, *Nature* **612**, 240 (2022).
- [20] P. Roushan, C. Neill, J. Tangpanitanon, V. M. Bastidas, A. Megrant, R. Barends, Y. Chen, Z. Chen, B. Chiaro, A. Dunsworth, A. Fowler, B. Foxen, M. Giustina, E. Jeffrey, J. Kelly, E. Lucero, J. Mutus, M. Neeley, C. Quintana, D. Sank, A. Vainsencher, J. Wenner, T. White, H. Neven, D. G. Angelakis, and J. Martinis, *Science* **358**, 1175 (2017).
- [21] Q. Guo, C. Cheng, H. Li, S. Xu, P. Zhang, Z. Wang, C. Song, W. Liu, W. Ren, H. Dong, R. Mondaini, and H. Wang, *Physical Review Letters* **127** (2021).
- [22] Q. Guo, C. Cheng, Z.-H. Sun, Z. Song, H. Li, Z. Wang, W. Ren, H. Dong, D. Zheng, Y.-R. Zhang, R. Mondaini, H. Fan, and H. Wang, *Nature Physics* **17**, 234–239 (2020).
- [23] J. Braumüller, A. H. Karamlou, Y. Yanay, B. Kannan, D. Kim, M. Kjaergaard, A. Melville, B. M. Niedzielski, Y. Sung, A. Vepsäläinen, R. Winik, J. L. Yoder, T. P. Orlando, S. Gustavsson, C. Tahan, and W. D. Oliver, *Nature Physics* **18**, 172 (2021).
- [24] P. Zhang, H. Dong, Y. Gao, L. Zhao, J. Hao, J.-Y. Desaulles, Q. Guo, J. Chen, J. Deng, B. Liu, W. Ren, Y. Yao, X. Zhang, S. Xu, K. Wang, F. Jin, X. Zhu, B. Zhang, H. Li, C. Song, Z. Wang, F. Liu, Z. Papić, L. Ying, H. Wang, and Y.-C. Lai, *Nature Physics* **19**, 120 (2022).
- [25] A. H. Karamlou, I. T. Rosen, S. E. Muschinske, C. N. Barrett, A. D. Paolo, L. Ding, P. M. Harrington, M. Hays, R. Das, D. K. Kim, B. M. Niedzielski, M. Schuldt, K. Serniak, M. E. Schwartz, J. L. Yoder, S. Gustavsson, Y. Yanay, J. A. Grover, and W. D. Oliver, Probing entanglement across the energy spectrum of a hard-core bose-hubbard lattice (2023), arXiv:2306.02571 [quant-ph].
- [26] A. J. Kollár, M. Fitzpatrick, and A. A. Houck, *Nature* **571**, 45–50 (2019).
- [27] J. G. Martinez, C. S. Chiu, B. M. Smitham, and A. A. Houck, *Science Advances* **9** (2023).
- [28] P. Roushan, C. Neill, A. Megrant, Y. Chen, R. Babbush, R. Barends, B. Campbell, Z. Chen, B. Chiaro, A. Dunsworth, A. Fowler, E. Jeffrey, J. Kelly, E. Lucero, J. Mutus, P. J. J. O'Malley, M. Neeley, C. Quintana, D. Sank, A. Vainsencher, J. Wenner, T. White, E. Kapit, H. Neven, and J. Martinis, *Nature Physics* **13**, 146 (2016).
- [29] M. Leib and M. J. Hartmann, *New Journal of Physics* **12**, 093031 (2010).
- [30] A. Biella, L. Mazza, I. Carusotto, D. Rossini, and R. Fazio, *Physical Review A* **91** (2015).
- [31] T. Mertz, I. Vasić, M. J. Hartmann, and W. Hofstetter, *Physical Review A* **94** (2016).
- [32] A. A. Bychek, P. S. Muraev, D. N. Maksimov, and A. R. Kolovsky, *Physical Review E* **101** (2020).
- [33] M. Fitzpatrick, N. M. Sundaresan, A. C. Li, J. Koch, and A. A. Houck, *Physical Review X* **7** (2017).
- [34] G. Fedorov, S. Remizov, D. Shapiro, W. Pogorov, E. Egorova, I. Tsitsilin, M. Andronik, A. Dobronosova, I. Rodionov, O. Astafiev, and A. Ustinov, *Physical Review Letters* **126** (2021).
- [35] A. Vrajitoarea, R. Belyansky, R. Lundgren, S. Whitsitt, A. V. Gorshkov, and A. A. Houck, Ultrastrong light-matter interaction in a multimode photonic crystal (2024), arXiv:2209.14972 [quant-ph].
- [36] S. Keßler and F. Marquardt, *Physical Review A* **89** (2014).
- [37] M. Atala, M. Aidelsburger, M. Lohse, J. T. Barreiro, B. Paredes, and I. Bloch, *Nature Physics* **10**, 588 (2014).
- [38] A. Impertro, S. Karch, J. F. Wienand, S. Huh, C. Schweizer, I. Bloch, and M. Aidelsburger, Local read-out and control of current and kinetic energy operators in optical lattices (2023), arXiv:2312.13268 [cond-mat.quant-gas].
- [39] J. Koch, T. M. Yu, J. Gambetta, A. A. Houck, D. I. Schuster, J. Majer, A. Blais, M. H. Devoret, S. M. Girvin, and R. J. Schoelkopf, *Physical Review A* **76** (2007).
- [40] W. S. Bakr, A. Peng, M. E. Tai, R. Ma, J. Simon, J. I. Gillen, S. Fölling, L. Pollet, and M. Greiner, *Science* **329**, 547 (2010).
- [41] R. O. Umucalılar and I. Carusotto, *Physical Review A* **96** (2017).
- [42] M. Hafezi, P. Adhikari, and J. M. Taylor, *Physical Review B* **92** (2015).
- [43] J. Lebreuilly and I. Carusotto, *Comptes Rendus Physique* **19**, 433 (2018).
- [44] R. Ma, C. Owens, A. Houck, D. I. Schuster, and J. Simon, *Physical Review A* **95** (2017).
- [45] S. de Léséleuc, V. Lienhard, P. Scholl, D. Barredo, S. Weber, N. Lang, H. P. Büchler, T. Lahaye, and A. Browaeys, *Science* **365**, 775 (2019).
- [46] G. T. Landi, D. Poletti, and G. Schaller, *Reviews of Modern Physics* **94** (2022).
- [47] B. Bertini, F. Heidrich-Meisner, C. Karrasch, T. Prosen, R. Steinigeweg, and M. Žnidarič, *Reviews of Modern Physics* **93** (2021).
- [48] F. Beaudoin, M. P. da Silva, Z. Dutton, and A. Blais, *Physical Review A* **86** (2012).
- [49] J. D. Strand, M. Ware, F. Beaudoin, T. A. Ohki, B. R. Johnson, A. Blais, and B. L. T. Plourde, *Physical Review B* **87** (2013).
- [50] Y. Lu, S. Chakram, N. Leung, N. Earnest, R. Naik, Z. Huang, P. Groszkowski, E. Kapit, J. Koch, and D. I.

- Schuster, Physical Review Letters **119** (2017).
- [51] C. Macklin, K. O'Brien, D. Hover, M. E. Schwartz, V. Bolkhovskiy, X. Zhang, W. D. Oliver, and I. Siddiqi, Science **350**, 307 (2015).
 - [52] R. K. Naik, N. Leung, S. Chakram, P. Groszkowski, Y. Lu, N. Earnest, D. C. McKay, J. Koch, and D. I. Schuster, Nature Communications **8** (2017).
 - [53] M. Reagor, C. B. Osborn, N. Tezak, A. Staley, G. Prawiroatmodjo, M. Scheer, N. Alidoust, E. A. Sete, N. Didier, M. P. da Silva, E. Acala, J. Angeles, A. Bestwick, M. Block, B. Bloom, A. Bradley, C. Bui, S. Caldwell, L. Capelluto, R. Chilcott, J. Cordova, G. Crossman, M. Curtis, S. Deshpande, T. E. Bouayadi, D. Girshovich, S. Hong, A. Hudson, P. Karalekas, K. Kuang, M. Lenihan, R. Manenti, T. Manning, J. Marshall, Y. Mohan, W. O'Brien, J. Otterbach, A. Papageorge, J.-P. Paquette, M. Pelstring, A. Polloreno, V. Rawat, C. A. Ryan, R. Renzas, N. Rubin, D. Russel, M. Rust, D. Scarabelli, M. Selvanayagam, R. Sinclair, R. Smith, M. Suska, T.-W. To, M. Vahidpour, N. Vodrahalli, T. Whyland, K. Yadav, W. Zeng, and C. T. Rigetti, Science Advances **4** (2018).
 - [54] G. Kordas, D. Witthaut, P. Buonsante, A. Vezzani, R. Burioni, A. I. Karanikas, and S. Wimberger, The European Physical Journal Special Topics **224**, 2127–2171 (2015).
 - [55] L. M. Sieberer, M. Buchhold, and S. Diehl, Reports on Progress in Physics **79**, 096001 (2016).
 - [56] S. Dutta and N. R. Cooper, Physical Review Research **3** (2021).
 - [57] *Thermodynamics in the Quantum Regime: Fundamental Aspects and New Directions* (Springer International Publishing, 2018).
 - [58] S. Deffner and S. Campbell, *Quantum Thermodynamics: An introduction to the thermodynamics of quantum information* (Morgan & Claypool Publishers, 2019).
 - [59] Z. Lenarčič, O. Alberton, A. Rosch, and E. Altman, Physical Review Letters **125** (2020).
 - [60] I. Klich and L. Levitov, Physical Review Letters **102** (2009).
 - [61] B. M. Anderson, R. Ma, C. Owens, D. I. Schuster, and J. Simon, Physical Review X **6** (2016).
 - [62] J. C. Owens, M. G. Panetta, B. Saxberg, G. Roberts, S. Chakram, R. Ma, A. Vrajitoarea, J. Simon, and D. I. Schuster, Nature Physics **18**, 1048 (2022).

Probing Site-Resolved Current in Strongly Interacting Superconducting Circuit Lattices

SUPPLEMENTARY MATERIAL

CONTENTS

A. Device Fabrication and Parameters	S1
B. Measurement Setup	S2
C. Experimental Control and Characterization	S2
C.1. Flux control and calibration	S2
C.1.i. DC flux crosstalk	S2
C.1.ii. Time domain characterization of flux control pulses	S2
C.2. Typical experimental sequence	S4
C.3. Qubit and Lattice Characterization	S5
C.4. Readout characterization	S5
D. Beamsplitter Operation for Measuring Current	S6
D.1. Non-interacting bosons	S6
D.2. Measuring current in the hardcore limit	S7
D.3. Calibrating the beamsplitter	S7
E. Coherent preparation of ground states	S8
E.1. Manybody spectra in the presence of driving	S8
E.2. Calibrating drive amplitude and phase	S10
E.3. Adiabaticity and many-body decoherence	S10
E.4. Effect of initial thermal population	S11
F. Bath-lattice coupling rates	S11
References	S12

A. DEVICE FABRICATION AND PARAMETERS

The superconducting circuit device used in this work consists of four frequency tunable transmon qubits [S1] in a linear array with fixed nearest-neighbor capacitive coupling, and individual readout resonators. The transmons have cross-shaped capacitors with $E_C \approx 2\pi \times 246$ MHz and flux tunable $E_J \approx 2\pi \times (9 - 18)$ GHz, corresponding to a tunable frequency of $\omega_{01} \approx 2\pi \times (4.0 - 5.7)$ GHz. The capacitance between the neighboring transmons $c \approx 0.2$ fF results in tunneling $J \approx 6$ MHz. The qubits are coupled to $\lambda/2$ coplanar-waveguide readout resonators with a coupling strength $g \approx 65$ MHz. The resonators are staggered in a frequency range of $6.18 - 6.32$ GHz, with a typical linewidth of 1.5 MHz. The flux bias lines are galvanically coupled to the SQUID loops of the transmon qubit with a mutual inductance $M \approx 0.86$ pH.

The device is fabricated using standard two-step lithography, at Purdue University's Birck Nanotechnology Center. The base layer is 150 nm of Niobium deposited using an e-beam evaporator (Plassys MEB550) on c -plane sapphire substrate. Optical lithography is performed with a direct pattern writer, followed by fluorine dry etching, to define all features on the chip except for the Josephson junctions. The Al/AlO_x/Al Josephson junctions are defined with e-beam lithography on MMA-PMMA bilayer resist, and deposited in the same e-beam evaporator using Manhattan style angled-evaporation. Ion milling prior to deposition ensures electrical contact between the Nb base layer and the Al junction traces. The bottom/top layers of Al are 50 nm/ 100 nm thick, deposited at 1 nm/s at an angle of 30° to normal. The junction oxidation is performed in $85\%/15\%$ A_r/O_2 for 10 minutes at 1 mBar. The frequency tunable transmons have two asymmetric junctions of sizes 130 nm \times 130 nm and 220 nm \times 220 nm. The junction SQUID loops have a dimension of 20 μ m \times 20 μ m.

The device is mounted to a multi-layer copper printed circuit board, and enclosed in a pocketed OFHC copper sample holder. Aluminum wire bonds are used to suppress stray on-chip modes, reduce signal crosstalk between control lines, and connect the chip to the printed circuit board. The packaged device is mounted inside a dual-layer mu-metal shield, and anchored to the base of a dilution refrigerator at 10 mK.

B. MEASUREMENT SETUP

The cryogenic setup is shown in Fig.S1(right). Low pass filters (K&L, Marki, Mini-circuit) and IR absorbers (Eccosorb CR-110, homemade) are used on all input and output coaxial lines to suppress noise and heating from high-frequency radiation. We use DC flux bias to control the idle frequency of the qubits using both on-chip flux lines, and an off-chip DC coil. The fast AC flux pulses, used to dynamically change the qubit frequencies during the experimental sequence, are combined with the DC flux on microwave bias tees at the mixing chamber. The bias-tees (Mini-circuit ZFBT-4R2GW+) have the capacitor on the rf port replaced by a short to allow the fast AC flux pulses to work down to DC. After passing through cryogenic circulators (Low Noise Factory), the readout output signal is amplified by a cryogenic HEMT amplifier (Low Noise Factory) and subsequently by additional room-temperature amplifiers.

The room temp control and measurement setups are shown in Fig.S1(left). A Quantum Machines OPX+ system provides multi-channel DC-coupled DAC outputs at 1GS/s, which are used directly for the fast AC flux pulses. Additional DAC outputs are used as I/Q signals and upconverted using IQ mixers (Marki) to generate qubit drive and readout pulses. Sideband flux control pulses used for bath engineering are generated similarly using IQ mixers near the required LO frequencies. After room temperature amplification and filtering, the frequency multiplexed readout signal from the fridge is downconverted with an I/Q mixer and recorded by the OPX+'s ADC at 1GS/s. This multiplexed heterodyne signal (centered around -120 MHz) is then digitally demodulated by the OPX+ to produce the I/Q signals for each qubit. Additionally, we generate digital pulses from the OPX+ to control fast microwave switches (Analog Devices ADRF5020) to avoid LO leakage when the pulses are idle. We use both low noise voltage sources (Analog Devices AD5780) and current sources (Yokogawa GS200) for applying the qubit DC flux bias.

C. EXPERIMENTAL CONTROL AND CHARACTERIZATION

C.1. Flux control and calibration

C.1.i. DC flux crosstalk

We observe relatively large crosstalk between our device's different flux control lines. A flux bias current I_j applied to the flux line for qubit j induces non-zero magnetic flux ϕ_i in the SQUID loops of all qubits i , due to the residual mutual inductance. To realize independent frequency control of each qubit, we measure the flux crosstalk matrix $M_{ij} = \partial\phi_i/\partial I_j$, defined from the flux response $d\phi_i = \sum_{j=1}^4 \frac{\partial\phi_i}{\partial I_j} dI_j$. The eigenvectors of the inverted crosstalk matrix M_{ij}^{-1} then provide the linear combinations of currents to independently tune each qubit to any desired flux value ϕ_i . The conversion between qubit frequency ω_i and flux ϕ_i is obtained by fitting the measured flux-dependent qubit spectra to a Jaynes-Cummings model.

The measured static dc flux crosstalk matrix is shown in Table S1, normalized row-wise to the diagonal elements. While the dc flux signals tune the qubits to their initial idle frequency, the fast-flux signals provide additional dynamic tuning with nanosecond resolution. In Table S2, we show the fast ac flux crosstalk matrix, measured from the time-averaged step-response to 3 μ s-long square fast-flux pulses. Improved flux line design and on-chip air bridges can reduce the overall flux crosstalk in future devices. We observe a frequency-dependent crosstalk of the fast flux control, which is a direct result of the different time-domain responses of the different flux lines. This suggests that part of the flux pulse distortion comes from the on-chip flux lines, which vary in length for each qubit. The time-domain characterization and compensation of the fast-flux pulses and crosstalk are detailed below.

C.1.ii. Time domain characterization of flux control pulses

Measuring the flux response: The fast-flux pulses generated by the room-temperature arbitrary waveform generators (QM OPX+, 1GS/s) can experience significant distortion when arriving at the qubit after passing through various lines, filters, and rf components. To characterize the distortion, we apply a square fast-flux pulse to a flux

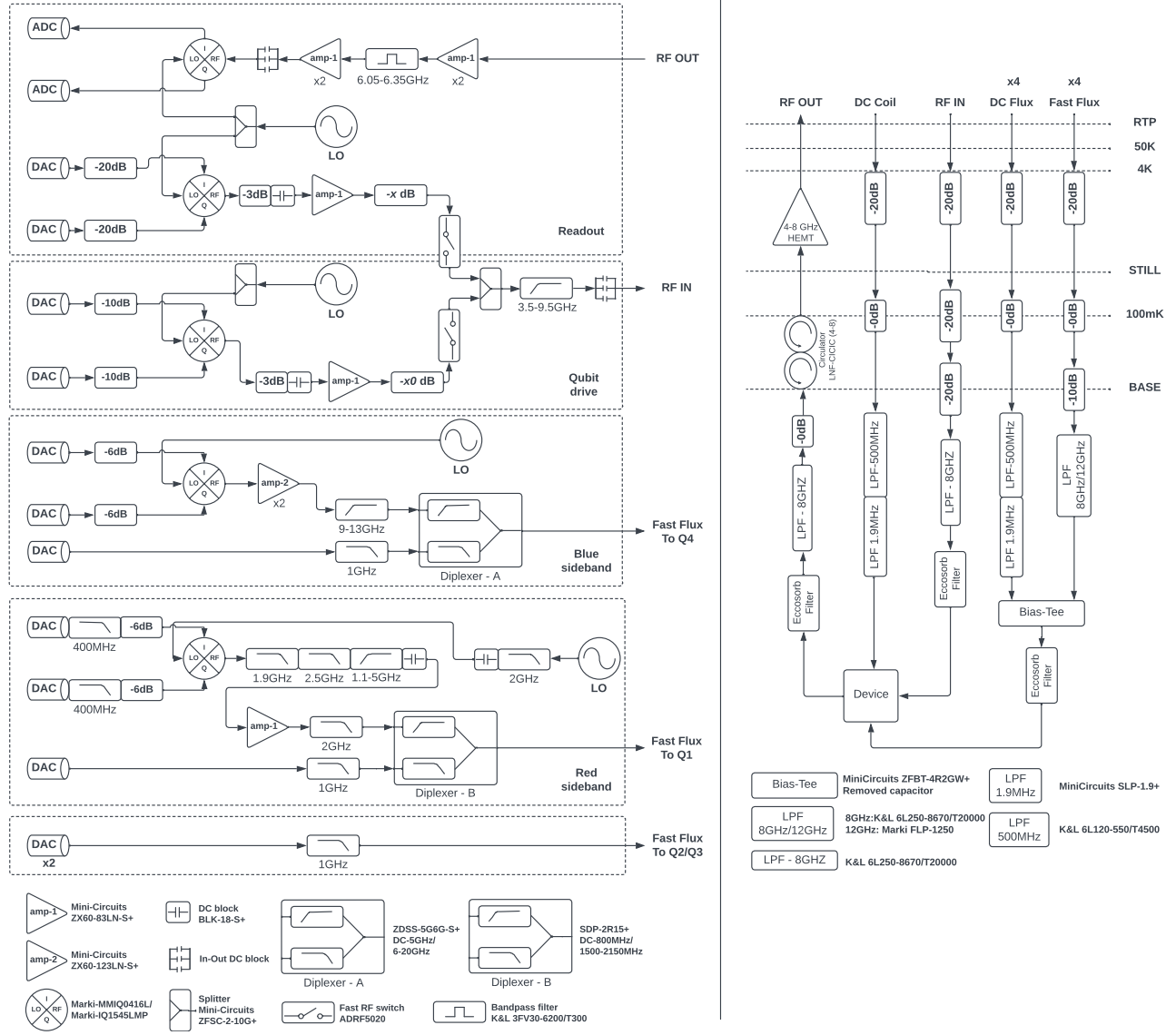


FIG. S1. Fridge wiring and measurement setup.

line and measure the frequency response of the qubit. The qubit frequency is measured using both Ramsey-type “CryoScope” experiments [S2] and pump-probe-type qubit spectroscopy experiments. The former provides time resolution at the pulse resolution of 1 ns but is limited to times shorter than the qubit dephasing time. The latter allows us to measure flux response at longer times, but the resolution is limited by the duration of the qubit excitation pulse to tens of ns.

The measured fast-flux response is shown in Fig. S2. The typical distortion shows a slow exponential rise with a decay constant of a few hundred ns, and fast oscillations with a period of few ns that decay in the first tens of ns. We attribute the former to the effective low-pass filtering effect of the filters and lines, and the latter to impedance mismatches near the on-chip flux lines. We measure an initial ramp time of ≈ 2 ns for all flux lines, see Fig. S2(c).

Flux pulse distortion compensation: We follow a procedure similar to that described in [S3]. We calculate the frequency response of the flux line from the measured time-domain step response, then take the Fourier transform of the inverted frequency response to construct a time-domain compensation kernel. To pre-compensate distortions in the flux line, the kernel is convoluted with the target flux pulse to generate the desired fast-flux waveform to be played on the pulse generators. All compensated pulses are computed off-line and then uploaded to the OPX+. We only compensate for distortions with time scales > 10 ns to reduce sensitivity to high-frequency noise in the step-response measurement and to retain the bandwidth of the fast flux pulse. The remaining fast oscillations at short

$$\partial\phi_i/\partial I_j$$

i \ j	1	2	3	4
1	1.0	-0.189	0.104	0.206
2	-0.317	1.0	0.059	0.261
3	-0.247	-0.267	1.0	0.287
4	-0.153	-0.153	-0.101	1.0

TABLE S1. Measured static flux (dc) crosstalk matrix.

$$\partial\phi_i/\partial I_j$$

i \ j	1	2	3	4
1	1.0	-0.028	0.044	0.031
2	-0.082	1.0	0.028	0.036
3	-0.056	-0.084	1.0	0.057
4	-0.031	-0.039	-0.083	1.0

TABLE S2. Measured fast-flux (ac) crosstalk matrix.

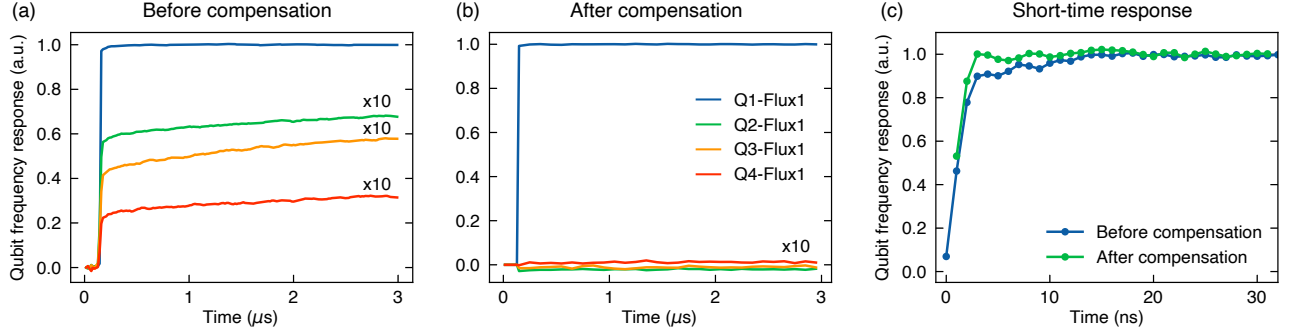


FIG. S2. Fast-flux pulse calibration and compensation. (a-b) Step responses before and after the time-dependent crosstalk compensation. The off-diagonal responses are plotted with same signs and on a $\times 10$ scale for easier visualization. (c) Typical short-time flux response before and after compensation.

times do not significantly affect the dynamics of the qubits in our experiments due to the relatively long tunneling time $2\pi/J \approx 160$ ns.

Time-dependent crosstalk: With relatively large flux crosstalk in the present device, we observe different step responses for all 4×4 qubit-to-flux-line pairs. This indicates non-negligible flux pulse distortion from on-chip structures. To achieve independent dynamical control of all qubits, we must compensate for a *time-dependent* crosstalk or, equivalently, a *frequency-dependent* crosstalk. From all 4×4 step responses, we calculate a frequency response matrix for all qubit-to-flux-line pairs and construct the corresponding time-domain kernel matrix to pre-compensate all fast-flux waveforms. In Fig. S2(a), we show the step responses of all qubits to the same flux line 1 with different time constants. The step responses after the time-dependent crosstalk compensation are shown in (b).

Net-zero flux pulses: We use net zero flux pulses for all experiment sequences to avoid the slow drifting of qubit frequencies due to the low-frequency response of the flux lines. This is realized by applying a flux-balancing pulse at the end of each experimental run so that the total area of the fast-flux pulse remains zero.

C.2. Typical experimental sequence

We start with all qubits tuned to the same frequency using dc flux bias, forming a degenerate lattice. The multi-qubit state in the lattice is then prepared in several ways: (1) Detune all qubits into a staggered frequency configuration using fast-flux pulses and apply resonant microwave pulses sequentially on each qubit via the readout transmission line; this is used for preparing the states in Fig. 2 of the main text and for preparing Fock states for readout calibration. The microwave pulses have a typical duration of 40 ns with a Gaussian width of $\sigma \approx 8$ ns. (2) Keep the qubits at the lattice frequency and directly apply a common microwave pulse that drives all qubits with time-varying amplitude and detuning; this is used in Fig. 3. (3) Apply fast-flux modulation pulses to select qubits to enable resonant coupling to the readout resonator, to realize a lattice with locally-coupled driven-dissipation baths. The bath populates the lattice with excitations. This is used in Fig. 4. After preparation, the many-body state can undergo an additional free evolution in the lattice with variable time to study their dynamics.

To probe the resulting state, we measure either the lattice density (on-site population of each qubit) or the current across two neighboring lattice sites (by performing the beamsplitter operation and then measuring the density).

	Q_1	Q_2	Q_3	Q_4
T_1 (μ s)	29	26	25	29
T_2^* (μ s)	2.7 - 3.0	2.2 - 2.7	1.0 - 2.2	1.5 - 2.5
$U/2\pi$ (MHz)	-246.5	-246.6	-246.4	-246.7
$J_{i,i+1}/2\pi$ (MHz)	5.78	5.80	5.86	n/a
n_{th}	0.064	0.059	0.056	0.052
$\omega_{read}/2\pi$ (GHz)	6.323	6.276	6.229	6.178
$g_{read}/2\pi$ (MHz)	67	65	64	65
$\kappa_{read}/2\pi$ (MHz)	1.5	1.5	1.5	1.6

TABLE S3. Measured device parameters.

When measuring current, the two sites of interest are rapidly tuned into resonance and undergo a controlled resonant tunneling, while all other qubits are detuned. All qubits are then moved rapidly to the staggered readout configuration. The frequency-multiplexed readout microwave pulse is applied for a typical duration of 1.5μ s. After the readout, the flux balancing pulses are applied to null the net current flowing into each flux line during the sequence.

The experiment is repeated with a cycle period of 300μ s, leaving enough idle time between sequences for the qubits to relax to their equilibrium ground states. Each sequence is run $\sim 40,000$ – $100,000$ times to accumulate statistics.

C.3. Qubit and Lattice Characterization

Table S3 lists the measured device parameters when the qubits are near the typical lattice frequency of 4.55 GHz. For performing multiplexed readout, the qubits are moved to staggered frequencies around (4.85, 4.40, 4.75, 4.30) GHz. The qubit relaxation times T_1 exhibit fluctuations up to a factor of 2 over time, while the dephasing times T_2^* are limited by the noise in the fast-flux signals from room temperature electronics. The tunneling rates J are measured from the oscillation of an initial excitation between two neighboring resonant sites. The effective interaction U , i.e. the anharmonicity of the transmon, is extracted from Ramsey experiments. The equilibrium thermal population of the qubits is measured from the amplitude of Rabi oscillation between the transmon excited states [S4]. We observe typical $n_{th} \approx 5.0$ – 6.5 %, corresponding to the effective qubit temperature of 70–80 mK. The thermal population can be reduced in future experiments with better microwave line filtering and improved sample package thermalization.

C.4. Readout characterization

We use a frequency multiplexed square pulse of length 1.5μ s for readout. The readout output signal, after hardware down-conversion, is digitally demodulated and integrated with constant weights to obtain the quadrature (I/Q) signals for each qubit. For simultaneous single-shot readout of all 4 qubits, the 4x2 I/Q signal is fed to a linear support vector machine (SVM) for state discrimination. The SVM [S5] is trained using calibration data by preparing the qubits in the basis states using resonant π pulses. Figure S3 shows the typical readout signal visualized in the I/Q plane of one readout resonator, and the assignment probability matrix for single-shot 4-qubit multiplexed readout.

Population in the transmon second excited state $n = 2$ (f -level) is negligibly small in the thermal ground state of the qubit. During the lattice experiments, any $n = 2$ population in the final state comes from Landau-Zener transfer between neighboring qubits as they are ramped from the lattice location to the readout location. We experimentally measure and numerically verify that this population transfer contributes to ≤ 1 % of readout error in our experiments. Hence we only include Fock states $n = 0, 1$ in the multiplexed readout.

We calculate the Fock state representation of a particular measured state by multiplying the SVM output probabilities with the inverted assignment probability matrix. Additionally, the prepared basis states include finite thermal populations. We use a linear transformation to map the state vector in the prepared basis state back to bare Fock states.

Readout error estimation: (1) The basis states for readout calibration are prepared using sequential resonant π -pulses at the readout location where all qubits are far detuned from each other. Typical measured π -pulse fidelities are 99.8 %. (2) Thermal population calibration. Throughout all experiments, we observed no significant change in the thermal population ($\lesssim 0.5$ %). The procedure we used above to extract the actual qubit state from readout calibration

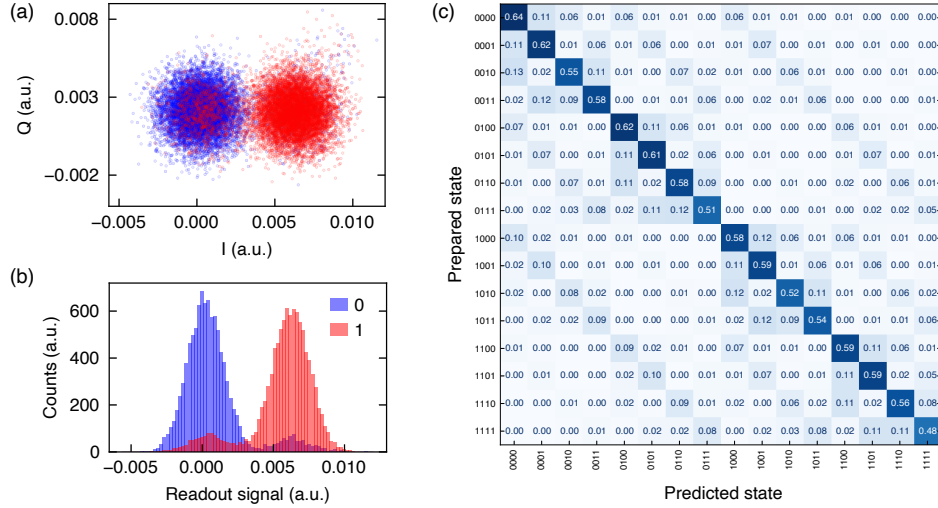


FIG. S3. Qubit readout. (a) Typical single-shot readout signal showing the distinguishability between qubit states in the I/Q space. In the 1D projection (b), we see $\sim 10\%$ in the opposite state due to contributions from the initial thermal population and measurement-induced qubit transitions. (c) Assignment fidelity matrix for 4-qubit multiplexed readout using linear SVM.

signal at finite temperature do not introduce any significant systematic readout errors. (3) Systematic uncertainties on the measured density and current due to Landau Zener transition are less than 1% [S6]. (4) With each experiment repeated for typically 40,000–100,000 times, the uncertainty from statistical error (standard error of the mean) is small compared to the contributions above.

D. BEAMSPLITTER OPERATION FOR MEASURING CURRENT

D.1. Non-interacting bosons

We first consider the time evolution of non-interacting bosons in a resonant double-well potential, with Hamiltonian $\mathcal{H}_{\text{dw}}/\hbar = J(a_l^\dagger a_r + a_r^\dagger a_l)$. The Heisenberg equations of motion reads

$$\frac{d}{dt}a_l(t) = -\frac{i}{\hbar}[a_l(t), \mathcal{H}_{\text{dw}}] = -iJa_r(t), \quad \text{similarly} \quad \frac{d}{dt}a_r(t) = -iJa_l(t).$$

These two differential equations can be solved, e.g. by a change of basis to the symmetric and anti-symmetric superpositions $(a_l \pm a_r)$ which are the eigenbasis of \mathcal{H}_{dw} . The results are

$$\begin{cases} a_r(t) = \cos(Jt)a_r(0) - i\sin(Jt)a_l(0) \\ a_l(t) = -i\sin(Jt)a_r(0) + \cos(Jt)a_l(0) \end{cases}$$

which simply describes the tunneling of bosons in the double-well potential. The time evolution of the density difference in the double-well can then be evaluated as

$$n_r(t) - n_l(t) = a_r^\dagger(t)a_r(t) - a_l^\dagger(t)a_l(t) = \cos(2Jt)[n_r(0) - n_l(0)] + i\sin(2Jt)[a_l^\dagger(0)a_r(0) - a_r^\dagger(0)a_l(0)]$$

The second term on the right can be identified as the current $\hat{j}_{l \rightarrow r} = iJ(a_l^\dagger a_r - a_r^\dagger a_l)$, to write

$$n_r(t) - n_l(t) = \cos(2Jt)[n_r(0) - n_l(0)] + \sin(2Jt)\frac{\hat{j}_{l \rightarrow r}(0)}{J}$$

For an evolution time of $t_{\text{BS}} = \pi/(4J)$, the first term proportional to the initial density difference vanishes. Therefore, we arrive at the conclusion that a non-interacting double-well at the chosen beamsplitter duration t_{BS} maps the current of the initial state to density difference after the evolution:

$$n_r(t_{\text{BS}}) - n_l(t_{\text{BS}}) = \frac{\hat{j}_{l \rightarrow r}(0)}{J}$$

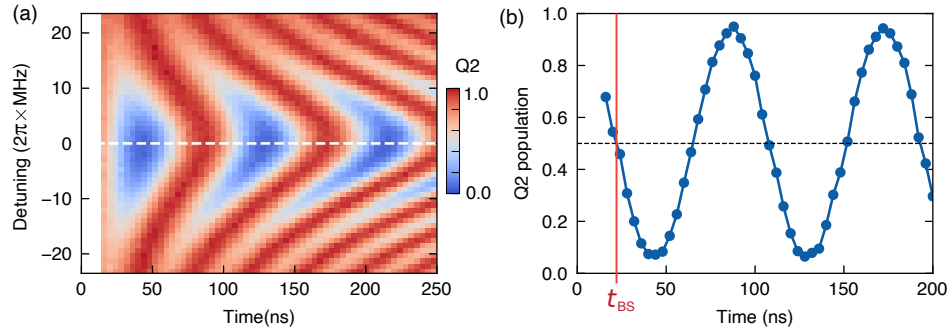


FIG. S4. Beamsplitter operation via resonant tunneling between two sites. (a) Population in one site as a function of time for different detuning between sites, (b) Resonant tunneling when the detuning is zero.

From here we see that the eigenvalues of $\hat{j}_{l \rightarrow r}$ are discrete and have values $j \in \{-nJ, -(n-1)J, \dots, +nJ\}$ where $n = n_l + n_r$. Measuring the distribution of density difference after the beamsplitter operation reveals the statistics of the current $P(j)$.

D.2. Measuring current in the hardcore limit

Our strongly interacting SC circuit lattice has fixed $|U/J| \gtrsim 40$ in the so-called hard-core boson limit. The mapping from current before the beamsplitter to on-site occupancy after the beamsplitter using the controlled tunneling in the hard-core boson limit is summarized as follows:

$$\begin{cases} P(j = +J) & \xrightarrow{\text{BS}} & P(|01\rangle) \\ P(j = 0) & \xrightarrow{\text{BS}} & P(|00\rangle) \\ P(j = -J) & \xrightarrow{\text{BS}} & P(|10\rangle) \\ P(j = -2J) & \xrightarrow{\text{BS}} & \frac{1}{2}P(|11\rangle) \\ P(j = +2J) & \xrightarrow{\text{BS}} & \frac{1}{2}P(|11\rangle) \end{cases}$$

For the hardcore Bose-Hubbard lattice with onsite occupancy limited to 0 or 1, the current can be written in terms of the Pauli operators:

$$\hat{j}_{l \rightarrow r} = iJ(\sigma_l^+ \sigma_r^- - \sigma_r^+ \sigma_l^-) = 2J(\sigma_l^x \sigma_r^y - \sigma_r^x \sigma_l^y)$$

This amounts to measuring two-qubit correlation functions, requiring phase-sensitive single-qubit rotations before readout as in [S7]. This seemingly simple approach turns out challenging for *analog* simulation experiments, where the qubits accumulate different phases during the continuous many-body evolution, and fully calibrating the phases for each qubit at each time step is extremely difficult. In contrast, our method is particularly suited for analog simulation experiments with frequency tunable lattice sites, eliminating the need to compensate for the phase accumulated during the evolution when applying the tomography pulses. We only measure onsite density after the controlled tunneling, which is phase-insensitive.

D.3. Calibrating the beamsplitter

The beamsplitter operation is a resonant tunneling between two neighboring sites for a duration of $\pi/4J$. This duration corresponds to a quarter period of the density oscillation for a single excitation initially localized in one site. We prepare the initial state at a detuning of $\approx 2\pi \times 150$ MHz, then rapidly tune the two sites near-resonance and measure the density after a variable time, as shown in Fig. S4. The vertical line marks the beamsplitter time t_{BS} . We use this same experiment to calibrate the lattice tunneling rate J .

E. COHERENT PREPARATION OF GROUND STATES

E.1. Manybody spectra in the presence of driving

Here we discuss the details of the state preparation scheme using the global coherent drive applied to all lattice sites. The driven Hamiltonian reads:

$$\mathcal{H}_d/\hbar = \mathcal{H}_{\text{BH}}/\hbar + \sum_i \frac{\Omega_d^i}{2} [a_i^\dagger e^{i\phi_i} + h.c.] - \Delta_d \sum_i n_i$$

where the Rabi rate Ω_d^i and phase ϕ_i can differ for different lattice sites. In our experiments, the microwave drive is applied through the common readout transmission line and goes through separate readout resonators to reach individual qubits. The detuning of the drive from the lattice frequency Δ_d resembles an effective chemical potential for the microwave photons.

Starting with an empty lattice, we would like to turn on the drive and sweep its detuning to go through avoided crossings that populate the lattice successively to different filling. To ensure adiabaticity, the rate of change of the drive frequency and amplitude must be slow compared to the instantaneous many-body gap at all times. We illustrate the requirements for adiabaticity by considering how the many-body gap depends on drive detuning, amplitude, and phase.

Effect of drive phase: The many-body gap reflects the effective coupling between many-body states under driving. It depends critically on the symmetry of the many-body states and the drive phase. The relative phases of the drive on different sites of the lattice determine the plausible adiabatic paths through the driven many-body spectra.

Consider the part of the adiabatic sweep where the lattice goes from empty to having one particle. As shown in the following sections, the global microwave drive has a near-uniform amplitude and phase when it reaches the different qubits in our present device. In addition, our capacitively coupled grounded transmon lattice has an alternating phase for the microwave field in the lowest energy single-particle eigenstate. Due to this different symmetry between the single particle wavefunction (with phase pattern $+ - + -$) and the drive (with phase pattern $+ + + +$), the effective rate to go from $n = 0$ to lowest energy $n = 1$ state will remain zero (gapless) even at finite driving amplitude. This is true for all transitions between lowest-energy states with different particle numbers. In Fig.S5(a) we show the many-body spectra when driving with uniform phase across the lattice. As the detuning is varied, the groundstate (red) transitions are all gapless, making it impossible to remain adiabatic when sweeping the drive detuning.

For the coherent filling of the lattice, we instead adiabatically follow the *highest* energy states of the system. These states in blue in Fig.S5(a) have uniform phase patterns $(+ + + +)$, opposite to the lowest energy states, making them always gapped under uniform phase driving. This drive sequence, used in the experiments in Fig. 3, is illustrated in Fig.S5(c): The solid path shows the drive used to prepare a fully filled $\bar{n} = 1$ lattice, while the dashed path indicates a drive sweep that ends at zero detuning and prepares the lattice at half filling $\bar{n} = 0.5$. For comparison, we plot in Fig.S5(b) the many-body spectrum in the case of uniform driving amplitude but staggered driving phases (i.e. π phase shift between neighbors). Now the lowest energy path is fully gapped and can be adiabatically prepared, while the highest energy states have the gap vanishing at a few detunings.

While we used a global drive with fixed relative amplitude and phase in the present experiments, we can readily implement individual qubit drives with independent amplitude and phase, by combining the charge driving signal with the flux bias signal [S8]. Generally, we expect local phase and amplitude-controlled driving to be a powerful tool for coherently preparing many-body states by selectively closing and opening level crossings in the many-body spectra.

Final states with vanishing many-body gaps: The adiabatic requirement cannot be met for final undriven states with a vanishing gap, which happens when the lowest energy states in two adjacent particle number manifolds are resonant in the rotating frame of the drive. This is shown in Fig.S5(d) where we plot the many-body gap at zero driving amplitude. When the end detuning of the drive is close to those values with a vanishing gap, we expect the state we prepare to be a superposition of two (nearly-) degenerate many-body eigenstates that differ in particle number by one. The exact details of the final state in our experiments are subject to further investigation. However, the current and current statistics we show in the main text at different lattice fillings are insensitive to the details of this superposition.

Normal modes in transmon lattices: We show that in our transmon array, when considering the phase of electric fields oscillating at the capacitor of each transmon qubit, the lowest-energy single-particle eigenstate in the lattice has alternating signs, i.e., electric field phase different of π between nearest neighbors). Meanwhile, the highest-energy single-particle eigenstate has uniform signs, i.e., the electric fields oscillate in phase on all qubits.

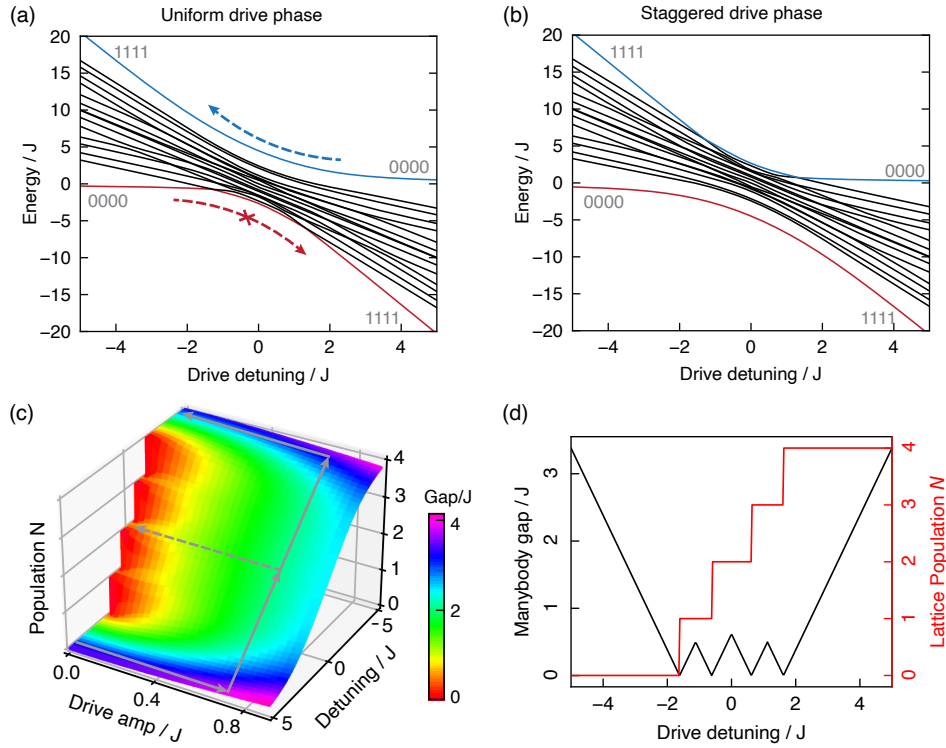


FIG. S5. Many-body spectra in the presence of coherent driving, for uniform (a) and staggered driving phases (b). The driving amplitude is $0.7J$ for all sites, matching the value used in our experiment. The drive phase determines whether the lowest (red) or highest (blue) states are gapped. (c) The paths taken by the coherent-driven preparation, where the end detuning determines the final lattice population. The many-body gap is shown in color to illustrate the adiabaticity requirements. (d) Many-body gap and lattice filling as a function of drive detuning at zero driving amplitude, i.e., the vertical cut in (c) at zero drive amplitude.

We use grounded transmons with direct capacitive coupling, represented by the effective circuit in Fig. S6(a). Focusing on single-particle states, we have ignored non-linearity from the Josephson junction and keep only the transmon capacitance C_0 , inductance L_0 , and coupling capacitance c . Solving Kirchoff's rules, the normal modes and frequencies for two resonantly coupled qubits are:

$$\begin{cases} \omega_+ = \frac{1}{\sqrt{L_0 C_0}} = \omega_0 & \text{with } V_1 = V_2 \\ \omega_- = \frac{1}{\sqrt{L_0 (C_0 + 2c)}} \approx \omega_0 (1 - \frac{c}{C_0}) = \omega_0 - 2J & \text{with } V_1 = -V_2 \end{cases}$$

where V is the voltage on the capacitor for each qubit. The mode '+' with $V_1 = V_2$ has no electric field in the coupling capacitor, hence the frequency is unchanged from the single qubit. The mode '-' with $V_1 = -V_2$ has a finite electric field in the coupling capacitance, lowering the curvature of the fields and hence lowering the energy. By the same argument, we see that the lowest-energy single particle eigenstate in the lattice will have the electric fields out of phase on neighboring sites, see Fig. S6(b). This corresponds to alternating signs relative to the individual qubit drive lines, which are also capacitively coupled to the qubit capacitors either directly or via the readout resonators.

The situation is different for a floating transmon array, depicted in Fig. S6(c). While the lowest, the spit capacitors for each qubit act as electric dipoles, making the electric fields to oscillate with the same phase for all qubits. The relative phase to the individual drive lines is now uniform.

Note that regardless of the circuit implementation, the node theorem always holds in 1D such that the lowest-energy state has no node in the electric field. The difference between the two configurations illustrated here can be alternatively viewed as having different signs for the effective tunneling J .

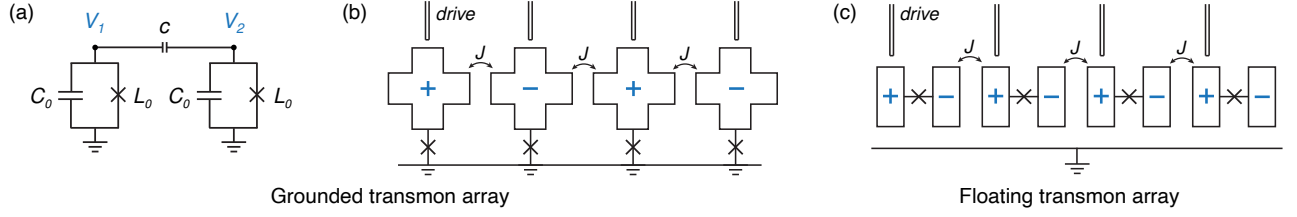


FIG. S6. Normal modes in transmon lattices. (a) Circuit diagram for coupled grounded transmons. (b) Relative signs of electric fields on the qubit capacitors for the lowest-energy single-excitation state.

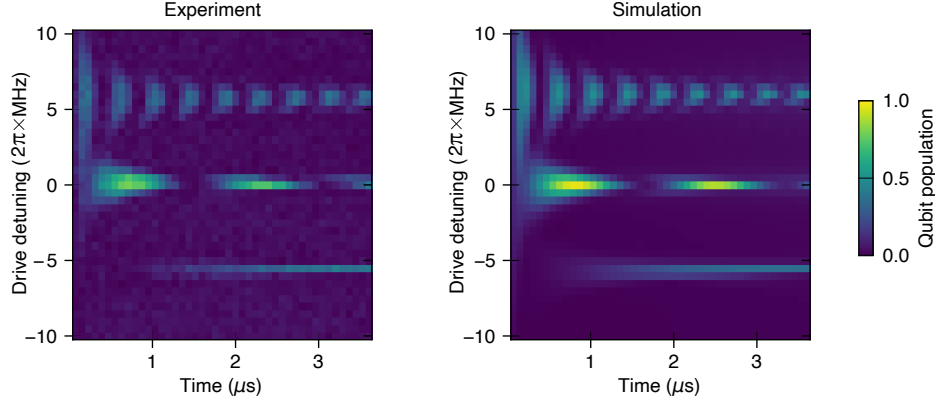


FIG. S7. Calibrate drive amplitude and phase. Population in left site after driving two resonantly coupled neighboring sites at different drive detuning and drive pulse duration.

E.2. Calibrating drive amplitude and phase

We measure the drive amplitudes Ω_d^i via Rabi oscillations of each qubit at the lattice frequency while other qubits are detuned away. The measured amplitudes are uniform across the lattice with less than 5% variation.

To estimate the difference in drive phases between neighboring sites, we measure the driven time evolution when the two sites are on-resonance. The one-excitation eigenmodes of the two-site system are $\frac{|01\rangle \pm |10\rangle}{\sqrt{2}}$, which are driven at effective rates that depend on the drive phase: $\Omega_d^\pm = (\Omega_d^L e^{i\phi_L} \pm \Omega_d^R e^{i\phi_R})/\sqrt{2}$. Here the label \pm on Ω follows the sign of the superposition, and according to the reasoning in the previous section, the ‘+’ state has higher energy than the ‘-’ state with a splitting of $2J$. In the limit where $\Omega_d^L \approx \Omega_d^R = \Omega_d$, the effective rates simplify to $|\Omega_d^-| = \sqrt{2}\Omega_d \cos(\theta/2)$ and $|\Omega_d^+| = \sqrt{2}\Omega_d \sin(\theta/2)$, where $\theta = |\phi_R - \phi_L|$. So by observing the Rabi frequencies of the two modes, we can extract the drive phase difference.

The data for the middle two sites of the lattice are shown in Fig. S7, where we plot the qubit population on one of the sites after applying a Gaussian pulse of varying length at different drive detuning. We observe the two single excitation resonances at drive detuning of $\pm J \approx 2\pi \times 6$ MHz. The highly suppressed Rabi rate Ω_d^- compared to Ω_d^+ indicates that the drive phase is almost identical for the two qubits. We fit the data to numerical simulations to extract $\theta \approx 7^\circ$. The additional resonance at zero detuning is a two-photon process oscillating between $|01\rangle$ and $|11\rangle$, enabled by a virtual transition through the detuned $|02\rangle$ and $|20\rangle$ states. We measure similar phase differences of 7° between all pairs of sites in our device. Overall we have a relatively uniform drive phase, approximately corresponding to the case in Fig. S5(a). The calibration method above does not reveal the sign of the phase difference. This sign can be extracted from an interferometer-type experiment between the two neighboring qubits [S8].

E.3. Adiabaticity and many-body decoherence

When maximizing the fidelity of the adiabatic preparation, the optimal rate of change for the drive detuning results from the competition between diabatic transitions when the rate is faster (shorter ramp duration), and decoherence when the rate is slower (longer ramp duration). We perform the state preparation by fixing the start and end frequency of the drive detuning ramp at $+2\pi \times 30$ MHz and $-2\pi \times 30$ MHz, and varying the duration of the linear ramp. In

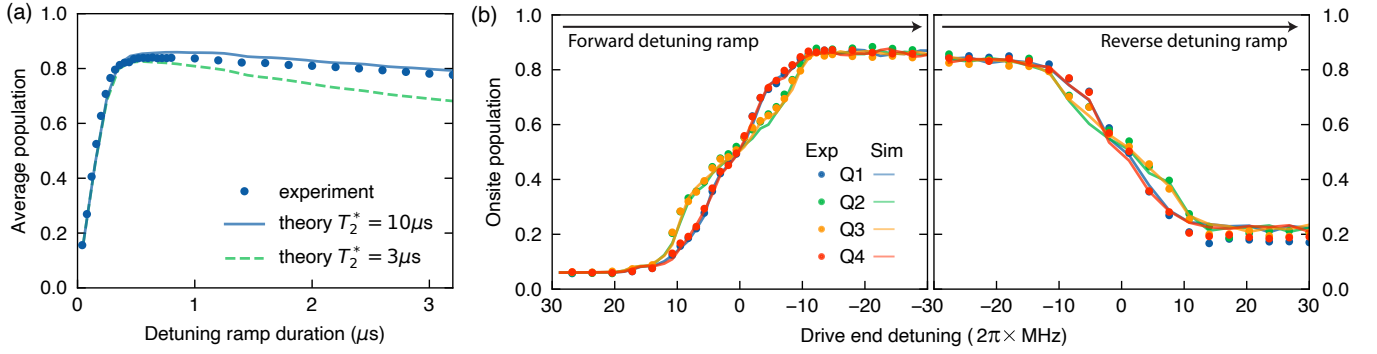


FIG. S8. Adiabaticity of the coherent preparation. Dots are experimental data, and lines are numerical simulations.

Fig. S8(a), we measure the final state average population \bar{n} as a function of the ramp duration. For ramp duration less than 500 ns, we see effects of diabatic transitions and a reduced fidelity for reaching the $\bar{n} = 1$ state. At durations larger than $1\mu s$, we observe reduced filling due to lattice relaxation and dephasing. We choose an optimal duration of 750 ns for the adiabatic preparation used in the main text, corresponding to a detuning ramp rate of $-2\pi \times 80 \text{ MHz}/\mu s$.

We show numerical simulations in good agreement with the observed data. The numerics are implemented in QuTiP by solving the Lindblad master equation. We use experimentally calibrated values for all coherent parameters, and the measured average single qubit lifetime at the lattice location $T_1 \approx 25\mu s$ for relaxation rate. When we include a white noise dephasing rate corresponding to the measured average single qubit $T_2^* \sim 3\mu s$, we see a significant over-estimation of decoherence in the numerical results, shown in Fig. S8(a). To match the adiabaticity data (and all other experimental data in the manuscript), we need to use a dephasing rate of $T_2^* \approx 10\mu s$ in the numerical calculations. Such suppressed effective many-body dephasing rate T_2^* has been observed in recent transmon lattice experiments [S9]. For the numerical simulation in Fig. S7(b), we used the same effective dephasing time of $10\mu s$.

Using the optimal ramp rate, we perform a “forward and back” experiment where we coherently drive from $\bar{n} = 0$ to $\bar{n} = 1$ then apply a second drive with a reversed detuning ramp to coherently bring the many-body system back to the initial state $\bar{n} = 0$. We vary the end detuning during the forward and back ramp and measure the onsite population after turning off the drive amplitude in 300 ns. The data is shown in Fig. S8(b)(right), where we have included the forward ramp data in Fig. 3 of the main text for comparison (left). Here the drive amplitude is turned to zero at the minimum detuning of $-2\pi \times 30 \text{ MHz}$, then turned back on before the reverse detuning ramp starts. Starting with an initial filling of 6% due to thermal population, we observe a final lattice filling of $\approx 20\%$ after the forward and back ramps. The numerical simulation, using the above mentioned many-body decoherence rates, show excellent agreement with the observed data. The initial state has $\approx 80\%$ probability in $|0000\rangle$, the final state after the forward ramp has $\approx 70\%$ probability in $|1111\rangle$, while the state after the forward-and-back ramp has $\approx 60\%$ probability in $|0000\rangle$.

E.4. Effect of initial thermal population

The lattice starts in an equilibrium ground state with a finite thermal population of approximately 6% on each lattice site. The thermal population can be coherently driven into different many-body eigenstates during the many-body preparation. In Fig. S9, we show numerical results to illustrate the distribution of the thermal components after the coherent preparation. We intentionally excluded decoherence effects in this calculation to focus on visualizing the coherent transfer of the initial thermal population across the many-body spectra. All numerical simulations in the manuscript include the effect of thermal population, in good agreement with experimental data.

F. BATH-LATTICE COUPLING RATES

The parametric modulation that enables the transmon-resonator coupling is applied via the local flux line of each transmon lattice site and induces a flux modulation of $\phi(t) = \phi_{\text{mod}} \cos(\omega_{\text{mod}} t) + \phi_0$ in the SQUID loop of the transmon. For relatively small modulation amplitude ϕ_{mod} around the lattice location we use, the transmon frequency is linearly dependent on the flux: $\omega_q(t) = \omega_0 + A_{\text{mod}} \cos(\omega_{\text{mod}} t)$. The Hamiltonian describing the capacitively coupled resonator

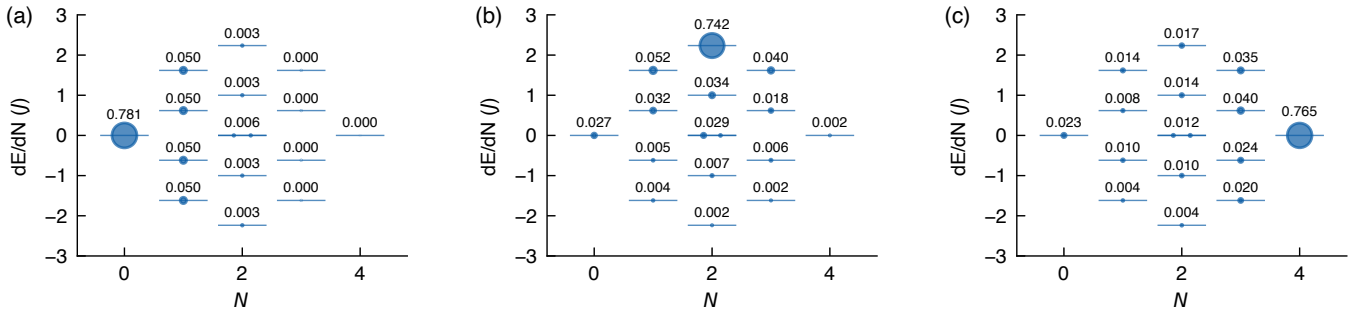


FIG. S9. Thermal population after the coherent preparation, from numerical simulations without decoherence. (a) The initial ground state. The numbers indicate probability in each many-body eigenstate. (b) Final state at half-filling. (c) Final state at unit-filling. Note there are two near-degenerate states at zero detuning for $N = 2$, where we show the total probability in both states.

and transmon system is:

$$H = \omega_q(t)a^\dagger a + \omega_r b^\dagger b + g(a^\dagger + a)(b^\dagger + b) + \frac{U}{2}a^\dagger a^\dagger aa$$

where b^\dagger is the creation operator for microwave photons in the resonator. The modulation frequencies that lead to the realization of effective particle drain (D) and particle source (S) are $\omega_{\text{mod}}^D \approx (\omega_r - \omega_q)$ (“red sideband”) and $\omega_{\text{mod}}^S \approx (\omega_r + \omega_q)$ (“blue sideband”). The red sideband modulation leads to an effective Hamiltonian with resonant tunneling between the qubit and resonator, written in the rotating frame of the qubit with the rotating wave approximation as:

$$H_{\text{red}} = g_D(a^\dagger b + b^\dagger a) + \frac{U}{2}a^\dagger a^\dagger aa$$

with effective red sideband coupling rate $g_D = J_1(\frac{A_{\text{mod}}}{|\omega_r - \omega_q|}) \times g$, where J_1 is the 1st order Bessel function of the first kind. On the other hand, the blue sideband modulation leads to an effective Hamiltonian:

$$H_{\text{blue}} = g_S(a^\dagger b^\dagger + ba) + \frac{U}{2}a^\dagger a^\dagger aa$$

with effective blue sideband coupling rate $g_S = J_1(\frac{A_{\text{mod}}}{|\omega_r + \omega_q|}) \times g$. The readout resonators in our device are dissipative with linewidth κ through their coupling to the common readout transmission line. This turns the above coherent sideband couplings into incoherent processes which we utilize as narrow-band particle drain and source.

In our experiments, to achieve a red sideband coupling rate of $g_D = 2\pi \times 2$ MHz, we used a sideband power of approximately -11 dBm before entering the fridge. This is consistent with analytical models and numerical simulations which predict a required flux modulation amplitude of $\phi_{\text{mod}} \approx 0.04\Phi_0$ at the lattice location, where Φ_0 is the magnetic flux quantum. This corresponds to a frequency modulation amplitude of $A_{\text{mod}} \approx 2\pi \times 115$ MHz. At the typical lattice location, the highest rate we can achieve in the present device is $g_D \approx 2\pi \times 12$ MHz, limited by the finite qubit frequency tuning range of approximately $2\pi \times (4 - 5.8)$ GHz.

To achieve a blue sideband coupling rate of up to $g_S = 2\pi \times 2$ MHz, we used modulation power up to 0.7 dBm before entering the fridge, in agreement with numerical modeling for $A_{\text{mod}} \approx 2\pi \times 640$ MHz. Due to the finite qubit frequency tuning range, the numerical model indicates a maximum $g_S \approx 2\pi \times 2.4$ MHz. Experimentally, we observed $g_S = 2\pi \times 4$ MHz with a sideband power of 7 dBm. We attribute this additional coupling to a three-wave mixing process enabled by a weak charge coupling between the flux line and the transmon. At higher modulation, we start to observe significant drive-induced heating of the transmon device.

During the flux modulation, the average qubit frequency will experience a shift coming from both the non-linear dependence of the qubit frequency on flux and drive-induced ac-Stark shifts. In our experiments, these shifts are on the order of a few MHz. To ensure the transmon sites remain at the lattice frequency when the baths are turned on, these shifts are measured and compensated using the dc component of the fast flux control.

[S1] Koch, J. *et al.* Charge-insensitive qubit design derived from the cooper pair box. *Physical Review A* **76** (2007).

- [S2] Rol, M. A. *et al.* Time-domain characterization and correction of on-chip distortion of control pulses in a quantum processor. *Applied Physics Letters* **116** (2020).
- [S3] Johnson, B. *Controlling photons in superconducting electrical circuits*. Ph.D. thesis, Yale (2011).
- [S4] Geerlings, K. *et al.* Demonstrating a driven reset protocol for a superconducting qubit. *Physical Review Letters* **110** (2013).
- [S5] Pedregosa, F. *et al.* Scikit-learn: Machine learning in Python. *Journal of Machine Learning Research* **12**, 2825–2830 (2011).
- [S6] Ma, R. *et al.* A dissipatively stabilized mott insulator of photons. *Nature* **566**, 51–57 (2019).
- [S7] Roushan, P. *et al.* Chiral ground-state currents of interacting photons in a synthetic magnetic field. *Nature Physics* **13**, 146–151 (2016).
- [S8] Karamlou, A. H. *et al.* Probing entanglement across the energy spectrum of a hard-core bose-hubbard lattice (2023). 2306.02571.
- [S9] Roberts, G. *et al.* Manybody interferometry of quantum fluids (2023).